Journal of Non-Newtonian Fluid Mechanics 345 (2025) 105469

Contents lists available at ScienceDirect

Journal of Non-Newtonian Fluid Mechanics

journal homepage: www.elsevier.com/locate/jnnfm

# The role of viscoelastic stress in an abruptly converging/diverging channel under the thin film approximation

M.H. Sari [a], H. Ahmed [a], C. Putignano [b], G. Carbone [b], L. Biancofiore [a,c,*]

[a] Mechanical Engineering Department, Bilkent University, 06800, Ankara, Turkey
[b] Department Mechanics, Mathematics and Management, Politecnico Di Bari, Bari, Italy
[c] Department of Industrial and Information Engineering, and Economics, University of L'Aquila, Piazzale Ernesto Pontieri, Monteluco di Roio, 67100 L'Aquila, Italy

ARTICLE INFO

*Keywords:*
Lubrication
Viscoelasticity
Thin film flows
Tribology

ABSTRACT

We analyze a viscoelastic fluid, modeled by the Oldroyd-B constitutive equation, flowing in a sliding abruptly converging/diverging channel. We have chosen this geometry since it has connections to the typical elastohydrodynamic lubricated (EHL), for which recently (Sarı et al., 2024) have illustrated how a viscoelastic lubricant has a positive effect on the tribological performance by raising load and decreasing friction coefficient. We assume that the channel is thin and the magnitude of the "jump" is small enough allowing to take advantage of the thin film approximation. We observe that the step location is a critical factor for generating viscoelastic pressure due to the positive and constant increase in the volumetric flow rate. Presence of viscoelasticity quantified by the ratio between fluid relaxation time and residence time, called Deborah number. A high Deborah number leads to a significant increment in pressure if the step is close to the inlet, while, if it is close to an outlet, the pressure decreases compared to Newtonian flows. While in most of the work, the pressure at the boundaries (inlet and outlet) is set to zero, we also tested more realistic boundary conditions in which the pressure is equal to the average elastic stress, showing that the two kinds of boundary conditions have a similar qualitative behavior. Lastly, a texture geometry, composed by one converging followed by one diverging steps, is inspected to mimic an EHL profile. We find what is the optimal distance between the steps to maximize the load. The role of the elastic stress in this texture profile is finally discussed.

## 1. Introduction

The onset of viscoelasticity can be observed in the flow of polymer enhanced fluids, e.g., lubricants, arising due to the special chemistry of the mixture. While the solvent remains Newtonian, acting as a substrate housing the complex polymers, the latter possess long chains of monomers that can stretch leading to interesting behavior. Over the years, extensive research has been conducted to comprehend polymer-induced viscoelasticity. This involves modeling microstructural states at a macroscopic-continuum scale and conducting experiments to assess its overall impact on flow fields in various contexts, including industrial and natural applications, such as, e.g., elastic turbulence, lubrication properties, flow in complex fluids and extrusion die processes [1–5]. Experiments measuring the properties of these mixtures, such as the relaxation time scale of the polymer, nonlinear dependence of viscosity on the flow kinematics (shear thinning, shear thickenning, viscoplasticity), often involve channel flows with varying geometries, either under pressure-driven (Poiseuille flow) or surface-driven (Couette flow) conditions.

Viscoelastic fluids, by their nature, pose significant challenges in modeling compared to Newtonian fluids due to the coupling of the (i) mass conservation, (ii) Cauchy's equation of motion, and (iii) a nonlinear constitutive equation describe the evolution of the polymeric stress [6]. Studies addressing viscoelasticity often entail numerical approaches. However, when the Weissenberg number $Wi$ (i.e., the ratio between fluid relaxation time and reference strain rate) is large, the governing system of equations for these problems inherit a critical numerical instability, i.e., the high Weissenberg number problem (HWNP), that prevents convergence. Fattal & Kupferman [7] showed that the HWNP is linked to the use of polynomial discretization methods. In order to tackle the numerical instabilities induced by this, analytical approaches have also been employed under limiting assumptions [8,9]. The behavior of viscoelasticity in abrupt contracting and

* Corresponding author at: Department of Industrial and Information Engineering, and Economics, University of L'Aquila, Piazzale Ernesto Pontieri, Monteluco di Roio, 67100 L'Aquila, Italy.
*E-mail address:* luca.biancofiore@univaq.it (L. Biancofiore).

https://doi.org/10.1016/j.jnnfm.2025.105469
Received 7 March 2025; Received in revised form 11 July 2025; Accepted 19 July 2025
Available online 7 August 2025
0377-0257/© 2025 The Authors. Published by Elsevier B.V. This is an open access article under the CC BY license (http://creativecommons.org/licenses/by/4.0/).

**Nomenclature**

| | |
|---|---|
| $\bar{\tau}_{xx}$ | Average elastic normal stress across $y$ |
| $\bar{\tau}_{xy}$ | Average elastic shear stress across $y$ |
| $\beta$ | solvent to total viscosity ratio |
| $\boldsymbol{\tau}$ | Stress tensor |
| $\boldsymbol{D}$ | Deformation tensor |
| $\boldsymbol{u}$ | Velocity field tensor |
| $\Delta h$ | height difference |
| $\ell$ | length of plateau for double step channel profile |
| $\epsilon$ | Height to length ratio |
| $\eta_o$ | solution viscosity |
| $\eta_p$ | polymer viscosity |
| $\lambda$ | polymer relaxation time |
| $\rho$ | Density of fluid |
| $\tau_{xx}$ | Elastic $x$-normal direction stress |
| $\tau_{xyE}$ | elastic shear stress |
| $\tau_{xy}$ | Shear stress |
| $\tau_{xy}^{V}$ | viscous shear stress |
| $\tau_{yy}$ | $y$-normal direction stress |
| $a$ | contraction/abruption location |
| $c$ | curvature of step |
| $De$ | Derborah Number |
| $h$ | height of fim thickness |
| $h'$ | the $x$ derivative of height |
| $h_{ref}$ | reference height |
| $p$ | pressure |
| $p_o$ | reference pressure |
| $p_N$ | pressure created by Newtonian viscosity |
| $p_{VE}$ | pressure created by viscoelasticity |
| $p_{xx}$ | pressure resulted by $\tau_{xx}$ |
| $p_{xy}$ | pressure resulted by $\tau_{xy}^{E}$ |
| $q$ | total volumetric flow rate |
| $q_C$ | volumetric flow rate resulted by Coutte flow |
| $q_N$ | volumetric flow rate resulted by $p_N$ |
| $q_{VE}$ | volumetric flow rate resulted by $p_{VE}$ |
| $t$ | Time |
| $u$ | $x$-direction velocity |
| $U_o$ | bottom surface velocity |
| $v$ | $y$-direction velocity |
| $W$ | load |
| $Wi$ | Weissenberg number |
| $x, y$ | Coordinate |

expanding channels is particularly studied to assess model accuracy and computational efficiency, given their simplistic geometry. At the channel inlet and outlet, the flow is assumed unidirectional (uniform along the streamwise direction), which simplifies the analyses, namely that the polymeric stress state is well defined in these regions. These analyses often focus on the viscoelasticity effect on changes in pressure and mass flow rate [9–11].

An extended investigation has been conducted to address the entrance problem with Newtonian, shear-thinning, and viscoelastic fluids both experimentally and numerically [12]. However, the assumption of creeping flow neglects shear-thinning due to the small shear-rate dependence. Nevertheless, the polymer stretching after the contraction and the subsequent tending to the relaxed state prompts further discussion on an additional pressure drop [13]. The downstream length

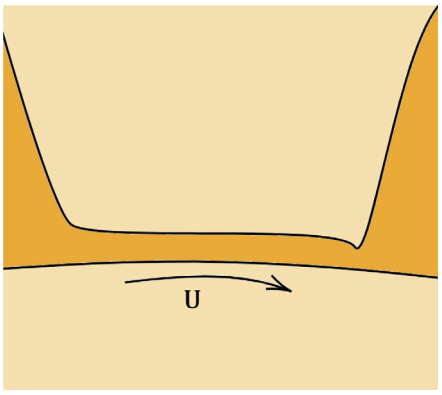


**Fig. 1.** A typical elastohydrodynamic profile in a sliding contact with wall velocity $U$.

significantly contributes to pressure drop, known as the Couette correction, owing to the relaxation of normal and shear stress. Particularly for larger Deborah numbers $De$ (i.e., the ratio between fluid relaxation time and residence time), polymer stretching extends towards the exit downstream, necessitating a sufficiently long downstream length to ensure an accurate Couette correction for obtaining the correct pressure drop. However, this extension can disrupt the numerical stability and accuracy of the lip vortex predictions [14–17].

The comprehensive examination of the overall pressure drop throughout the channel has not been extensively explored. Instead, the downstream stress relaxation is often addressed through the Couette correction rather than solving for the full-scale pressure–velocity coupling. Generally, there is a lack of consensus on determination of the exit channel length for a contraction–expansion geometry, except for the need to ensure fully developed exit conditions [9,18,19]. It is also noteworthy that in the assumption of creep flow, discussions about the location of contraction for viscoelastic fluids are absent. In particular, the significant impact of viscoelastic stress on flow dynamics in various thin film contacts and shear flows has not been addressed in previous studies.

Modeling lubricant flow through thin contacts via reduced-order models is attained by perturbing the flow in the Deborah number and has been extensively explored for the well-known Oldroyd-B constitutive equations for various geometries [20–24]. Analytical solutions are available up to $O(De^3)$ with reciprocal theorem, while velocity field corrections up to $O(De^2)$ accurately predict viscoelastic stress and pressure in the low $De$ in smooth hyperbolic pressure-driven channels [25]. Another study dealing with a similar non-sliding channel, extends analytical expression up to $O(De^8)$ with high order asymptotic methods for various viscoelastic models in addition to Oldroyd-B [23].

Under the thin film approximation in sliding contacts numerous studies use perturbation theory to reduce the viscoelastic models which are only limited to small $De$ [20,21,24]. A numerical algorithm called viscoelastic Reynolds (VR) proved to be successful for solving Oldroyd-B and FENE-type models for larger $De$ (or $Wi$), aligning well with Direct Numerical Simulation (DNS) results [26,27]. VR estimates viscoelastic normal and shear stress accurately even at moderate to high $Wi$ numbers, thereby delaying mesh-dependent issues associated with the HWNP, which imposes strict stability conditions on numerical modeling [3,28]. A particular geometry of sliding contacts appears in elastohydrodynamic lubrication (EHL) profile which was recently studied in combination with viscoelastic lubricants [24]. A typical EHL profile has a flat surface in the middle sandwiched by two abrupt varying portions of the channel (one converging and one diverging), as illustrated in Fig. 1. It was found that when the applied force was high, viscoelasticity is more effective (i) in enhancing the load carrying capacity of the lubricant and (ii) in decreasing friction. As a result the channel is further flattened, and, as a consequence, the surface

gradients before and after the flat regions are enhanced. Therefore, an analysis on viscoelastic lubricant sliding in an abrupt converging/diverging channel can also shed light on the improved tribological performance in EHL contacts due to the fluid viscoelasticity.

In contrast with previous works, where a fully pressure-driven flow was analyzed in a smoothly varying channels, allowing for meaningful analytical expressions for relation between the pressure drop and flow rate [23,29–31], here, we examine numerically using the VR approach, the effect of a sharply varying profile and normal stresses. Aside from EHL profiles, many applications involving thin lubricating films contain sharply varying surface features, such as surface textures, surface roughness, and pocketed pads to cite a few [21,32–34] For these cases, obtaining analytical expressions is quite challenging owing to the singular surface derivatives. Our paper is structured as follows; Section 2 introduces the geometry and includes the scaling of the equations, while Section 3 focuses on the results of our simulations, focusing in particular on the pressure change and the equivalent volumetric flow rates. Finally, in Section 4 we conclude and discussed our findings.

## 2. Mathematical model and geometry

The particular focus of this study lies in examining a thin, straight channel with a small contraction or expansion. The lower surface slides with a constant velocity $U$, while the upper surface is stationary. From lubrication theory the analytical solution for a Newtonian fluid is known [35] and gives a constant pressure gradient across the channel. By employing a constant volumetric flow rate per unit depth, $q$, the pressure gradient can be obtained without considering the impulse induced by the contraction. The same approach will be applied to the viscoelastic lubricant to discern its behavior around the step location. Although an analytical solution is available for the non-Newtonian pressure at the inlet before disturbing the flow, the small contraction induces elongation of the polymeric chains. This must be taken numerically into account to further explore the pressure gradient behavior, as the analytical expression alone is insufficient to explain the evolution of elastic normal and shear stress. In Section 2.1 we introduce the governing equations used in this work and particularly the VR approach [26,27], while in Section 2.2 the profile will be described and commented.

### 2.1. Governing equations

The equations governing the flow of a viscoelastic lubricant through a thin channel are (i) the mass conservation

$$\nabla^* \cdot \boldsymbol{u}^* = 0, \tag{1}$$

where, $\boldsymbol{u}^*$ is the velocity, (ii) the Cauchy's equation of motion

$$\frac{\partial \boldsymbol{u}^*}{\partial t^*} + (\boldsymbol{u}^* \cdot \nabla^*)\boldsymbol{u}^* = -\nabla^* p^* + \nabla^* \cdot \boldsymbol{\sigma}^*, \tag{2}$$

where, $p^*$ is the pressure, $\boldsymbol{\sigma}^* = \boldsymbol{\tau}_s^* + \boldsymbol{\tau}^*$ is the total stress tensor, $\boldsymbol{\tau}_s^*$ is the Newtonian solvent stress, $\boldsymbol{\tau}^*$ is the polymeric extra stress, and (iii) a constitutive relation for the polymer stress. In this work we chose the Oldroyd-B constitutive relation

$$\boldsymbol{\tau}^* + \lambda \overset{\nabla^*}{\boldsymbol{\tau}} = 2\eta_p \boldsymbol{D}^*, \quad \text{and} \quad \boldsymbol{D}^* = \frac{1}{2}(\nabla^* \boldsymbol{u}^* + \nabla^* \boldsymbol{u}^{T*}) \tag{3}$$

where, $\lambda$ is the polymer relaxation time and $\eta_p$ is the polymer viscosity, and $\overset{\nabla^*}{\boldsymbol{\tau}} = \frac{\partial \boldsymbol{\tau}^*}{\partial t^*} + u^* \cdot \nabla^* \boldsymbol{\tau}^* - \boldsymbol{\tau}^* \nabla^* \boldsymbol{u}^* - \nabla^* \boldsymbol{u}^{*T} \boldsymbol{\tau}^*$ is the upper convected time derivative. The Oldroyd-B describes the spatial and temporal growth of the dilute polymer solution in which the polymer is approximated as a dumbbell that can stretch infinitely [28].

We apply lubrication theory by (i) substituting the scaling and selecting $h_{ref}$ as the maximum height of the channel

$$x = \frac{x^*}{L}, \quad y = \frac{y^*}{h_{ref}}, \quad u = \frac{u^*}{U_o}, \quad v = \frac{v^*}{\epsilon U_o}, \quad \epsilon = h_{ref}/L, \quad t = t^* \frac{U_o}{L},$$

$$\tau_{xx} = \tau_{xx}^* \frac{h_{ref}^2}{\eta_o U_o L}, \quad \tau_{xy} = \tau_{xy}^* \frac{h_{ref}}{\eta_o U_o}, \quad \tau_{yy} = \tau_{yy}^* \frac{L}{\eta_o U_o}, \quad p = (p^* - p_0)\frac{h_{ref}^2}{\eta_o U_o L}, \tag{4}$$

where, $\epsilon$ is the thin film ratio, and (ii) neglecting all terms on the order of $\epsilon^2$ to get a thin-film reduced system of equations,

$$\frac{\partial u}{\partial x} + \frac{\partial v}{\partial y} = 0, \tag{5a}$$

$$\frac{\partial p}{\partial x} = \beta\left(\frac{\partial^2 u}{\partial y^2}\right) + \frac{\partial \tau_{xx}}{\partial x} + \frac{\partial \tau_{yx}}{\partial y}, \tag{5b}$$

$$\frac{\partial p}{\partial y} = 0, \tag{5c}$$

$$\tau_{xx} + De\left(\frac{D\tau_{xx}}{Dt} - 2\tau_{xy}\frac{\partial u}{\partial y} - 2\tau_{xx}\frac{\partial u}{\partial x}\right) = 0, \tag{5d}$$

$$\tau_{xy} + De\left(\frac{D\tau_{xy}}{Dt} - \tau_{yy}\frac{\partial u}{\partial y} - \tau_{xx}\frac{\partial v}{\partial x}\right) = (1-\beta)\frac{\partial u}{\partial y}, \tag{5e}$$

$$\tau_{yy} + De\left(\frac{D\tau_{yy}}{Dt} - 2\tau_{xy}\frac{\partial v}{\partial x} - 2\tau_{yy}\frac{\partial v}{\partial y}\right) = 2(1-\beta)\frac{\partial v}{\partial y}. \tag{5f}$$

By non-dimensionalizing the equations two important parameters emerge, namely the (i) Deborah number $De = \lambda U/L$, i.e., the ratio of the polymer relaxation time and the residence time scale and (ii) $\beta = \eta_s/(\eta_s + \eta_p)$ the viscosity concentration ratio. The boundary conditions are

$$u(x,0) = 1, \; u(x,h) = 0, \tag{6a}$$

$$v(x,0) = 0, \; v(x,h) = 0, \tag{6b}$$

$$p(0) = 0, \; p(1) = 0, \tag{6c}$$

where, pressure at the inlet and outlet are set to zero gauge pressure. The pressure boundary conditions are reevaluated in the following sections of the paper taking into account the polymer normal stress. Assuming the flow originates from a flat channel with a constant pressure gradient equal to that at the inlet, we can write

$$\begin{bmatrix} \tau_{xx}(0,y) \\ \tau_{xy}(0,y) \\ \tau_{yy}(0,y) \end{bmatrix} = \begin{bmatrix} 2De(1-\beta)(\frac{\partial u}{\partial y})^2 \\ (1-\beta)\frac{\partial u}{\partial y} \\ 0 \end{bmatrix}. \tag{7}$$

Along the upper wall, $u(x,h) = v(x,h) = 0$ which simplifies the stress components into a set of equations in terms of $\frac{\partial u}{\partial y}$, $\dot{\gamma} = \frac{\partial u}{\partial y}(x,h)$ at wall and $h'$:

$$\begin{bmatrix} \tau_{xx}(x,h) \\ \tau_{xy}(x,h) \\ \tau_{yy}(x,h) \end{bmatrix} = \begin{bmatrix} 2De(1-\beta)\dot{\gamma}^2 \\ (1-\beta)(1+2De h'\dot{\gamma})\dot{\gamma} \\ 2(1-\beta)(1+De h'\dot{\gamma})h'\dot{\gamma} \end{bmatrix}. \tag{8}$$

The detailed derivation of the stress boundary conditions (Eqs. (7)–(8)) is given in Appendix A.

The direct numerical simulation (DNS) of the governing equations is computationally expensive and limited to small values of the Deborah number due to the HWNP. The numerical solution of the thin-film reduced system is equally difficult because of the coupling of the pressure and velocity (partially remedied by the invariance of the pressure across the film). To overcome these limitations, several studies employ the classical perturbation methods in $De$ [20,23,31], the reciprocal theorem [22,36] or the viscoelastic Reynolds (VR) approach [26,27]. We employ the latter since it exploits the weak linear dependence of the velocity field on the Deborah number [37] but allows for the stress to be nonlinear and coupled. The solution for the pressure comes from the solution of Eq. (5b) and this yields a Reynolds type equation

$$\begin{aligned} \frac{d}{dx}\left(\frac{h^3}{12}\frac{dp}{dx}\right) = \frac{\beta}{2}\frac{dh}{dx} &+ \frac{d}{dx}\left(\int_0^h \frac{y}{h}\int_0^h\int_0^y \frac{\partial \tau_{xx}}{\partial x}dy''dy'dy \right. \\ &\left. - \int_0^h\int_0^y\int_0^y \frac{\partial \tau_{xx}}{\partial x}dy''dy'dy\right) \\ &+ \frac{d}{dx}\left(\int_0^h \frac{y}{h}\int_0^h \tau_{xy}dy'dy - \int_0^h\int_0^y \tau_{xy}dy'dy\right), \end{aligned} \tag{9}$$

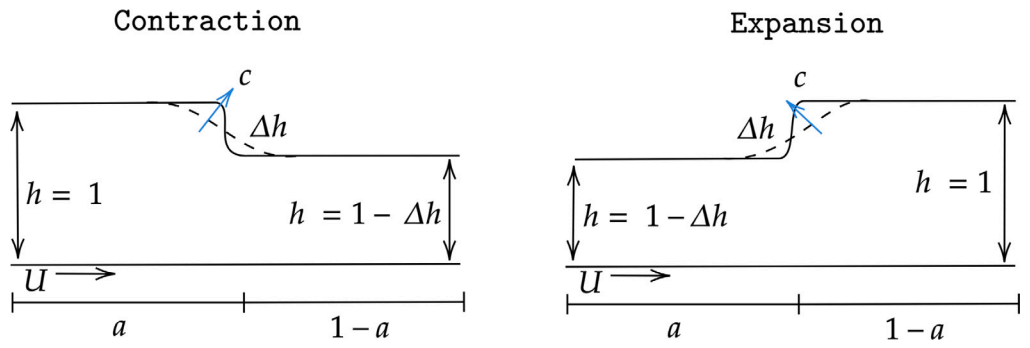


**Fig. 2.** The step geometry in which $a$ is the location of the step, $\Delta h$ is the difference in height between the channel entrance and exit, and $c$ (see Eq. (11)) is a parameter that adjusts the steepness of the step.

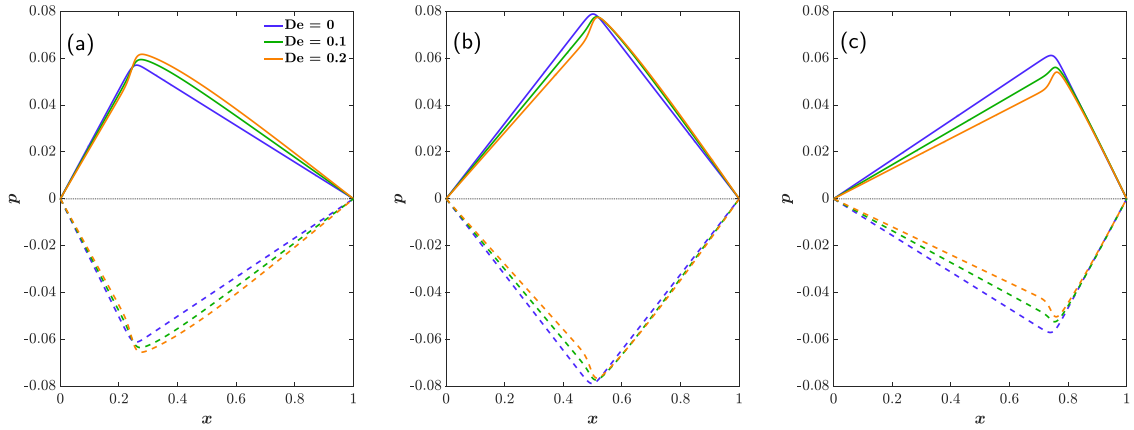


**Fig. 3.** The pressure distribution along the channel for different Deborah numbers examined for three different locations of the step; (a) $a = 0.25$, (b) $a = 0.5$, (c) $a = 0.75$, solid line (-) for $\Delta h = 0.025$ and dashed line (- -) $\Delta h = -0.025$. Note that $\beta = 0.5$.

coupled with Eqs. (5)(d-f). In order to decouple the stress and the velocity, we exploit the weak dependence of the latter on the Deborah number. The velocity field is obtained from the linearized solution in $De$ [20,21,24]

$$\boldsymbol{u} = \boldsymbol{u}^0 + De\boldsymbol{u}^1. \tag{10}$$

For the expressions of $\boldsymbol{u}^0$ and $\boldsymbol{u}^1$, see Appendix B. This approach was validated in lubricated contacts against direct numerical solutions over a moderate range of $De$, see Refs. [26,27] for more details. The velocity field up to $De$-order, Eq. (10), is used (i) to decouple the Oldroyd-B stress, Eq. (5)(d-e), from the pressure and (ii) evaluate the boundary conditions depicted by Eqs. (7)–(8). Using Eq. (9), the pressure is calculated directly by the calculated extra stress tensor.

### 2.2. Geometry

The channel surface profile consists of two straight parallel sections joined via a smoothened step defined by

$$h(x) = 1 - \frac{\Delta h}{2} - \text{sign}(\Delta h)\frac{\Delta h}{2}\tanh(c(x-a)), \tag{11}$$

where $a$ is the step location and $\Delta h$ is the jump between the two straight sections. The steepness of the abruptly converging/diverging region depends on the parameter $c$, as shown schematically in Fig. 2. After comparisons with DNS (see Appendix C), a value of $c = 60$ is chosen to ensure that $\partial p/\partial y = 0$ in accordance with lubrication theory.

## 3. Results

In this section, we use the viscoelastic Reynolds numerical approach to obtain the pressure distributions for varying step configurations, varying the location of the step, $a$, and the depth of protrusion, $\Delta h$. In Section 3.1, we examine how the streamwise normal component of the polymer extra stress influences the pressure distribution and, subsequently, the load carrying capacity. Afterwards we analyze the effect of viscoelasticity on the volumetric flow rate in Section 3.2. We also examine the effect of finite normal stresses at the channel boundaries in Section 3.3 comparing the results with the classical Newtonian condition, and, finally, in Section 3.4, we analyze the same quantities for a surface geometry mimicking the EHL channel. Note that in all our simulations we set $\beta = 0.5$ and we have chosen the step locations sufficiently far ($0.25 \leq a \leq 0.75$) from the channel inlet and outlet in order to avoid any boundary effects and finite pressure in those regions.

### 3.1. Pressure and load carrying capacity

The pressure distribution ultimately determines the net force produced by the film which is defined in this work as

$$W = \int_0^1 p \, \mathrm{dx}. \tag{12}$$

In Eq. (12), the contribution of the cross-film polymer normal stress, $\tau_{yy}$, is omitted because it is $O(\epsilon^2)$. For lubricated contacts $W$ must balance the applied load otherwise the surfaces can come into contact leading to wear and frictional losses.

In Fig. 3, we show the pressure distribution along the channel for different values of the Deborah number varying the location of the step (a) $a = 0.25$, (b) $a = 0.5$ and (c) $a = 0.75$. The dashed lines represent an expanding step, while the solid lines indicate a converging step.

In general for converging steps, we find the pressure increasing downstream of the step but decreasing upstream. On the other hand,

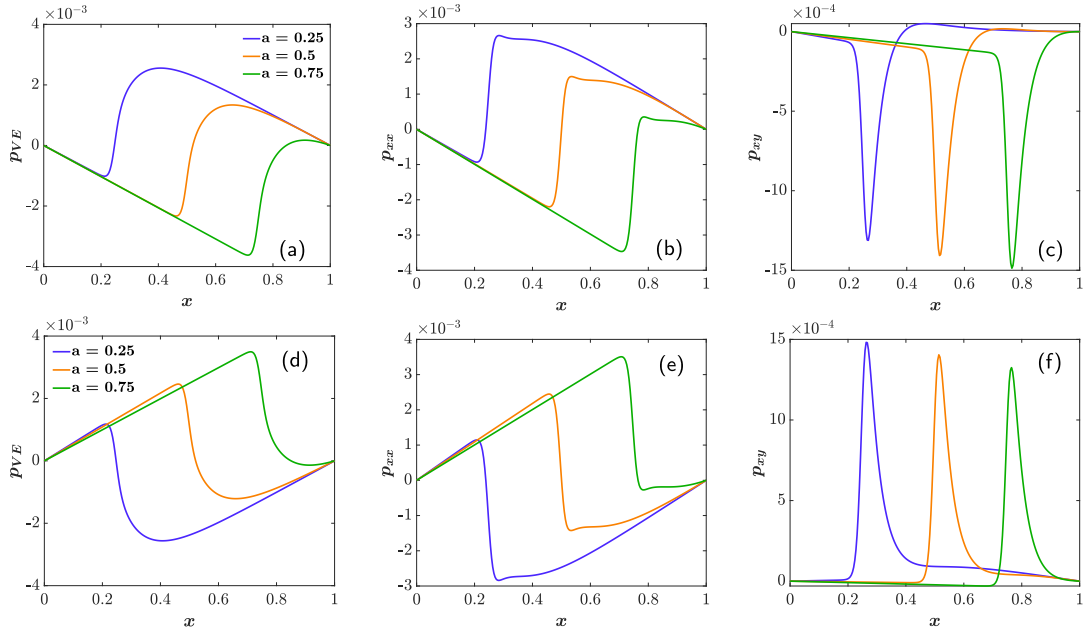


**Fig. 4.** The distribution of (a) the total viscoelastic pressure $p_{VE}$, (b) the pressure due to normal stresses and (c) the pressure due to the polymeric shear stress for a positive step $\Delta h = 0.025$. The same components are also plotted in (c)–(f) for a negative step $\Delta h = -0.025$ ($De = 0.1$ and $\beta = 0.5$).

for diverging steps, we see the opposite effect (i.e, pressure decreasing downstream of the jump, while increasing upstream). These behaviors are due to (1) the advection of the polymer due to stretching (considered as a dumbbell, its two ends stretch into different shearing zones giving the impression of stress transport) and (2) as pointed out by Hinch et al. [30], the growth of the normal stress upstream relieves the pressure by supplying part of the necessary force needed to propel the fluid. Downstream, the normal stresses decrease causing the pressure to rise in order to maintain constant the flow rate. As the step is placed closer to the channel exit, the region in which the pressure tends to decrease (increase) for negative (positive) $\Delta h$ is larger creating a total net decrease of the load carrying capacity. If we consider the extension of the polymers as the main mechanism for the load increase, then the room available to stretch for the polymers in Fig. 3(c) is the least, thereby preventing the polymers from reaching their maximum stretched state (controlled via the applied shear rate which is the same in all cases).

Solving for the pressure in Eq. (9), we can define the Newtonian and total contribution of viscoelasticity to the pressure, $p_N$ and $p_{VE}$, respectively

$$\frac{d}{dx}\left(\frac{h^3}{12}\frac{dp_N}{dx}\right) = \frac{1}{2}\frac{\partial h}{\partial x} \tag{13a}$$

$$p_{VE} = p_{xx} + p_{xy}, \tag{13b}$$

where $p_{xx}$ and $p_{xy}$ are the contributions of the normal stress and the polymer shear stress, respectively, to the pressure

$$\frac{d}{dx}\left(\frac{h^3}{12}\frac{dp_{xx}}{dx}\right) = \frac{d}{dx}\left(\int_0^h \frac{y}{h}\int_0^h\int_0^y \frac{\partial \tau_{xx}}{\partial x}dy''dy'dy - \int_0^h\int_0^y\int_0^y \frac{\partial \tau_{xx}}{\partial x}dy''dy'dy\right) \tag{14a}$$

$$\frac{d}{dx}\left(\frac{h^3}{12}\frac{dp_{xy}}{dx}\right) = \frac{d}{dx}\left(\int_0^h \frac{y}{h}\int_0^h \tau^E_{xy}dy'dy - \int_0^h\int_0^y \tau^E_{xy}dy'dy\right) \tag{14b}$$

where the shear stress is split into its viscous and elastic parts such that

$$\tau^E_{xy} = \tau_{xy} - \tau^V_{xy} = \tau_{xy} - (1-\beta)\frac{\partial u}{\partial y}, \tag{15}$$

and $\tau_{xx} = \tau^E_{xx}$ as the viscous part of the normal stress is zero under the lubrication approximation.

In Fig. 4, we plot $p_{VE}$, $p_{xx}$ and $p_{xy}$ for different values of the step location and depth. Figs. 4(a)–(c) correspond to a converging step and 4(d)–(f) correspond to a diverging step. Overall, it appears that $p_{VE}$. $p_{xx}$ and $p_{xy}$ have same order of magnitude for the two examined values of $\Delta h$. For the contracting geometry, $p_{xx}$ decreases linearly until reaching the step. At the step location the polymers stretch and alter the pressure profile. The same behavior is observed for the expanding channel, but with opposite sign. The effect of the shear stress on the pressure is weaker, since $p_{xy}$ is in general lower than $p_{xx}$. Only around the jump, in which a sharp peak of $p_{xy}$ is present (negative for positive $\Delta h$ and positive for negative $\Delta h$), the two components have the same order of magnitude.

Our analysis continues with reporting in Fig. 5(a) the load $W$ versus the Deborah number and (b) the contours in the plane ($\Delta h$, $a$) of $W - W_N$ where $W_N$ is the Newtonian load $W_N = \int_0^1 p_N dx$. Note that in (b) $W$ is calculated at $De = 0.1$. In Fig. 5(a), we find that, for a positive $\Delta h$, the load increases versus $De$ only when the step is placed close to the inlet ($a = 0.25$). For a step placed in the center and close to the exit ($a = 0.5$ and $a = 0.75$, respectively), the load tends to decrease. The trends are reversed when the channel is diverging, i.e., $\Delta h < 0$. It is important to note that the onset of viscoelasticity strongly depends on the location of the step, which can also be observed in Fig. 3. Recent studies by Boyko et al. [29] and Hinch et al. [30] highlight the importance of the exit and entrance lengths of the channels and their effect on polymer relaxation. This is reflected in the pressure profiles and, subsequently, on the load. Upon closer inspection of Fig. 5b, one can observe that around $a = 0.5$, the difference $W - W^N$ is zero and the generated load decreases when the step is located near the inlet or the outlet.

In the flat region, the pressure gradient dies out, and the only remaining part is the Couette-driven flow, where $\frac{\partial u}{\partial y} = -\frac{1}{h}$, scaled with the channel height. The normal stress is found considering, there is no pressure gradient in this flat region

$$\tau_{xx} = 2(1-\beta)De\left(\frac{\partial u}{\partial y}\right)^2 = 2(1-\beta)De\frac{1}{h^2} \tag{16}$$

showing that $\tau_{xx}$ is proportional to $\frac{1}{h^2}$. This means that $\bar{\tau}_{xx} = \frac{1}{h}\int_0^h \tau_{xx}dy$ scales with $\frac{1}{h^2}$ as well. Thus, $\bar{\tau}_{xx} = 0.1De$ when the height equals

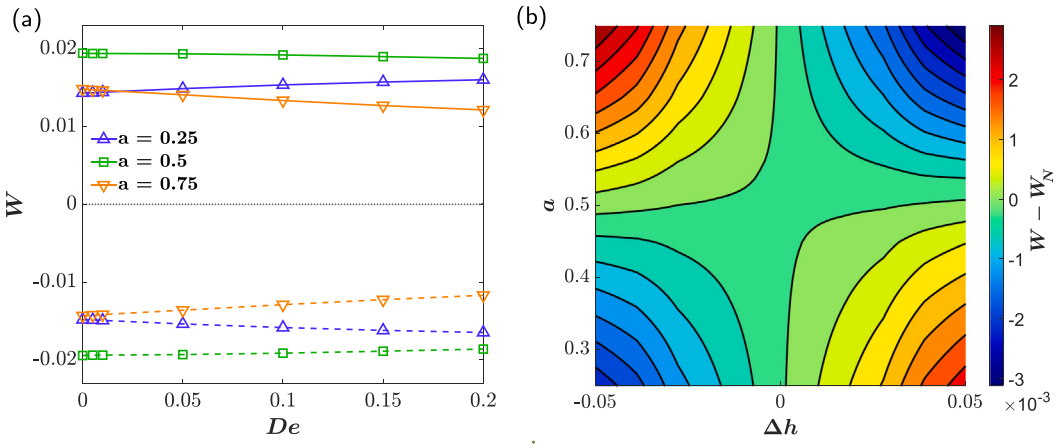


**Fig. 5.** (a) The load values with respect to $De$ with various step locations. Positive loads (continuous lines) corresponds to $\Delta h = 0.025$ and negative loads (dashed lines) to $\Delta h = -0.025$. (b) Contours of the difference between total load $W$ and Newtonian load $W_N$ for different values of the step location $a$ and $\Delta h$ values ($De = 0.1$ and $\beta = 0.5$).

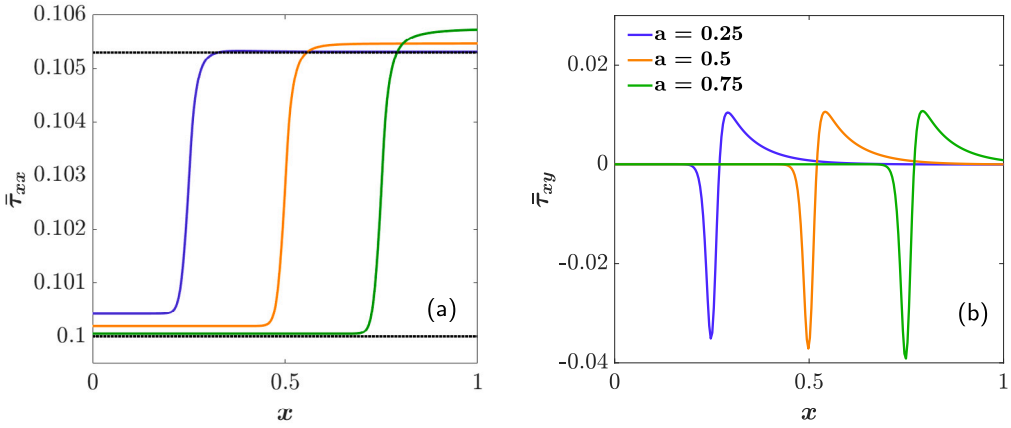


**Fig. 6.** The distribution of the film-averaged (a) streamwise normal stress $\bar{\tau}_{xx}$ and (b) the shear stress $\bar{\tau}_{xy} = \frac{1}{h}\int_0^h \tau_{xy} dy$ for $De = 0.1$ and $\beta = 0.5$. The dotted lines represent the value of the stresses corresponding to that of a perfectly flat sliding channel.

unity, and in general after the jump, the film averaged normal stress is $\bar{\tau}_{xx} = \frac{1}{(1+\Delta h)^2} De$.

We illustrated in Fig. 6 how the film averaged (a) normal and (b) shear stress evolve along the domain for different values of $a$ and $\Delta h = 0.025$. The values of the stresses corresponding to a flat channel are reported by dotted lines. From the entry to the step location (from the step location to the exit), the elastic stresses are equal to the nominal stress values for a flat channel if the step is located far enough from the inlet (outlet). For $a = 0.75$, the average stress is larger indicating a insufficient room for relaxation.

In Fig. 6(b) we notice that the average polymeric shear stress, unlike the Newtonian solvent stress, carries an advective component due to the polymer stretch. Not surprisingly, it experiences pulses at the location of the step. However, their magnitude depends on the location with the highest value recorded for $a = 0.75$. This again alludes to a build-up of the shear stress from the stretched polymers upstream which is advected downstream.

### 3.2. Volumetric flow rate

In this section, we analyze how the volumetric flow rate depends on the elastic stress and the viscoelastic pressure. The volumetric flow rate per unit length, $q$, is calculated by integrating the velocity field, $u$, across the film

$$q = \int_0^y u \, dy. \tag{17}$$

The expression for volumetric flow rate, is obtained by integrating (thrice) the $x$-momentum equation across the film, Eq. (5b). Inserting the equivalent viscous shear stress (Eq. (15)) and carrying out the integration, the volumetric flow rate is

$$\begin{aligned} q = -h^3 \frac{dp}{dx} + 6h + 12 \Bigg( \int_0^h \frac{y}{h} \int_0^h \int_0^y \frac{\partial \tau_{xx}}{\partial x} dy'' dy' dy \\ - \int_0^h \int_0^y \int_0^y \frac{\partial \tau_{xx}}{\partial x} dy'' dy' dy \Bigg) \\ + 12 \left( \int_0^h \frac{y}{h} \int_0^h \tau_{xy}^E dy' dy - \int_0^h \int_0^y \tau_{xy}^E dy' dy \right). \end{aligned} \tag{18}$$

The flow rate carries three contributions. The first term being the Poiseuille contribution, second term the Couette contribution, and the third term involving the integral expressions is the elastic stress contribution. Particularly, at the entrance of the flat channel, the elastic contribution is exactly zero due to the boundary condition (Eq. (7)). At the inlet $\tau_{xy} = (1-\beta)\frac{\partial u}{\partial y}$ resulting $\tau_{xy}^E = 0$ as shear stress only contains viscous part.

Note that channels satisfying $h(x_{inlet}) = h(x_{outlet})$ yield a purely Newtonian flow field [26,38]. Although the step profile considered here deviates from this condition, the small depth of the step $\Delta h \ll 1$ gives a velocity field that is weakly dependent on the Deborah number. The transport due to the viscoelastic pressure is significant in contrast to the first-order flow rate correction, i.e., $q^{(1)} = \int_0^h De\, u^{(1)} dy$, which is negligible and not included in $p_{VE}$ when the channel inlet and outlet

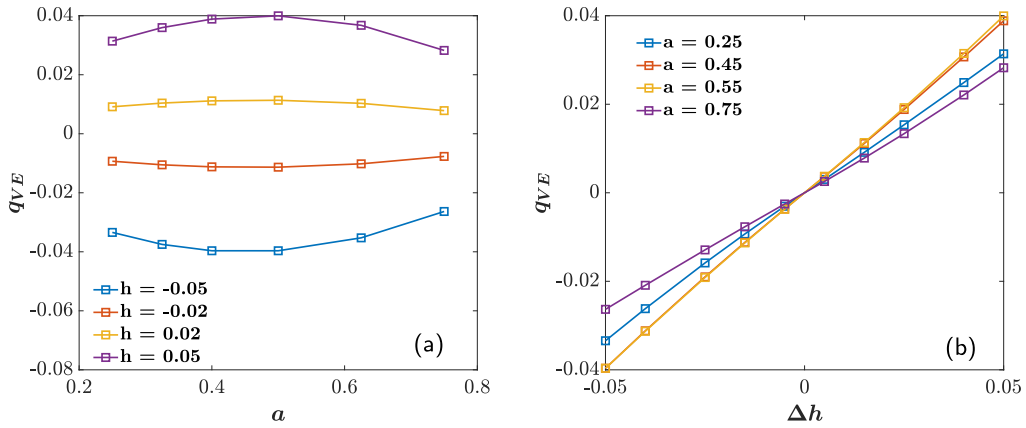


**Fig. 7.** The Poiseuille component of the volumetric flow rate versus (a) the location of the step and (b) the depth of the step using $De = 0.1$ and $\beta = 0.5$.

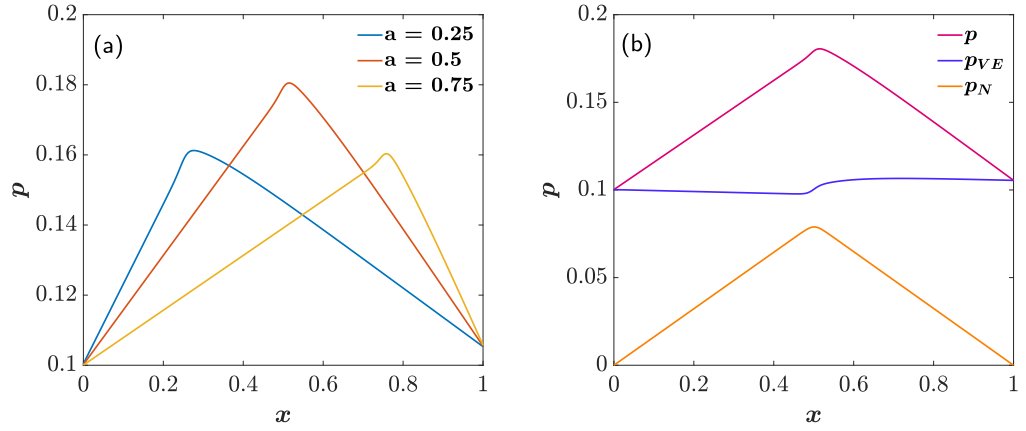


**Fig. 8.** The pressure distribution, using Eqs. (20) as boundary conditions, along the channel for (a) different locations of the step and (b) a comparison with the Newtonian symmetric pressure distribution for the step fixed at $a = 0.5$ using $\Delta h = 0.025$, $De = 0.1$ and $\beta = 0.5$. .

heights differ slightly ($\Delta h \ll 1$). The mathematical expression of $q^{(1)}$ can be found in Appendix B.

After eliminating the elastic terms, the total volume flow rate $q$ is split as the sum of the pressure driven (Poiseuille), both Newtonian and viscoelastic, and the Couette term $q = q_N + q_{VE} + q_C$. By utilizing solutions of pressures given in Eqs. (13) and (14), volumetric flow rates are expressed as

$$q_N = -h^3 \frac{dp_N}{dx}, \quad q_{VE} = -h^3 \frac{dp_{VE}}{dx} \quad \text{and} \quad q_C = 6h. \tag{19}$$

In Fig. 7, we focus on showing the mass flow due to viscoelastic pressure, $q_{VE}$, versus the step location $a$ and depth $\Delta h$. The pressure pushing the fluid back in the contraction and the opposite in expansion. Interestingly, the location of the step has a nonlinear influence on the viscoelastic flow rate resulted by $p_{VE}$, exhibiting a concave shape, as seen in Fig. 7(a), whereas, it changes linearly versus changing step size, as shown in Fig. 7(b). Also, considering the pressure gradients shown in Fig. 4(a-d), we can deduce that $q_{VE}$ is not a strong function of the step location. In contraction case ($\Delta h > 0$), the pressure resulted due to the elastic stresses, transports more fluid into the channel, independent of the step location. This aligns with the findings of Boyko et al. [29] and Hinch et al. [30]. The fluid transported by the elastic normal stress is the main factor in decreasing the pressure gradient, and vice versa in expansion cases.

### 3.3. Pressure boundary conditions

In this section, we examine how the additional polymer normal stress at the channel inlet and outlet can influence the pressure for the step configuration. For an ultra-dilute mixture in which the polymer concentration is very small, the normal stresses are weak compared to the bulk pressure. Similarly, for small Deborah numbers, the pressure along the channel greatly exceeds the normal stress at the boundaries and one can assume a constant pressure, close to the ambient conditions, at the boundaries. Assuming a force balance across the channel inlet and outlet interface, we find that the pressure is given by the average normal stress

$$p = \frac{1}{1 + \min(0, \Delta h)} \int_0^{1+\min(0,\Delta h)} \tau_{xx}(x = 0, y)\, dy, \quad \text{at} \quad x = 0 \tag{20a}$$

$$p = \frac{1}{1 + \min(0, -\Delta h)} \int_0^{1+\min(0,-\Delta h)} \tau_{xx}(x = 1, y)\, dy, \quad \text{at} \quad x = 1. \tag{20b}$$

Eqs. (20) serve only as a remedy, since the true normal stress varies across the channel, whereas the pressure does not.

Using Eqs. (20) as inlet and outlet pressure boundary conditions, we plot the pressure profile along the channel for different step configurations in Fig. 8(a). Accounting for the additional elastic stress leads to a greater pressure along the channel. In contrast to the purely pressure driven flow, a long enough channel would lead to a decay in the normal stress, and, therefore, a relaxation of the stretched polymer chains. In the boundary driven case, regardless of the channel length, the sliding action of the surface induces a Couette flow component that does not vanish, leading to a prevailing rate of deformation (or shear $\dot{\gamma}$) and a finite normal stress that scales with $\dot{\gamma}^2$. In Fig. 8(b), we fix the step and decompose the pressure into its Newtonian solvent and viscoelastic polymeric parts for $a = 0.5$. The new pressure boundary conditions account for a significant increase and, once again, the loss of symmetry in the pressure distribution due to the stretching of the

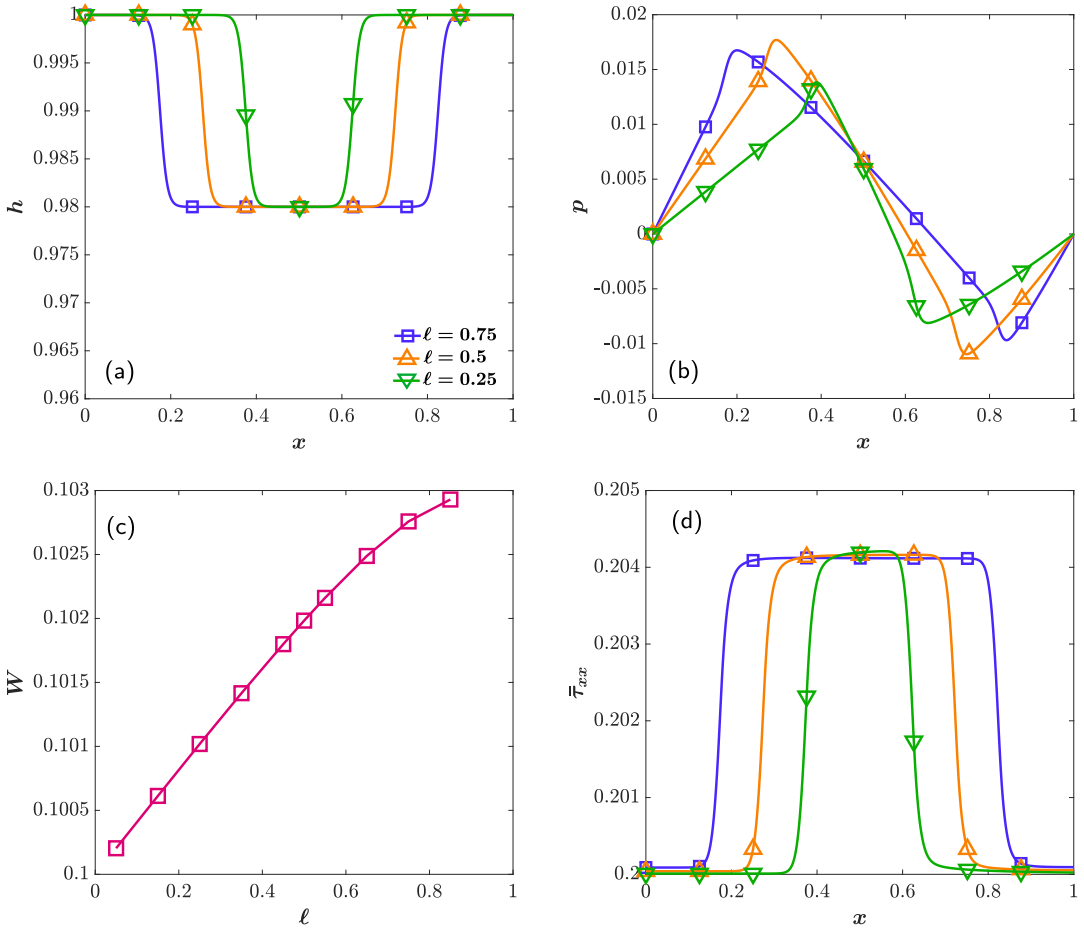


**Fig. 9.** (a) The double step profile for different values of $\ell$ (with $\Delta h = 0.02$). (b) The pressure distribution for the profiles depicted in (a). (c). Load carrying capacity vs $\ell$ for the double step profile. (d) Normal stress $\tau_{xx}$ distribution for the profiles depicted in (a). Note that $De = 0.1$ and $\beta = 0.5$ in Figs. (b), (c) and (d).

polymeric chains causing the stress to be advected across the flow, leads to a finite increase in the load carrying capacity.

### 3.4. Double step profile

Thus far, we have examined the flow of a viscoelastic lubricant as it encounters a sharp step or protrusion. Here, we extend it and consider a channel mimicking the plateau formed by an elasto-hydrodynamically lubricated contact under pressure. Its key feature is a constant inlet and outlet height but a large section flattened due to the force exerted by the lubricant, as shown in Fig. 9(a). The length of the plateau is denoted by $\ell$, and its depth is kept constant at $\Delta h = 0.02$.

Previous studies for polymeric extrusion have shown the strong influence of relaxation time (or equivalently the distance over which it can relax [29]. In Fig. 9(b) we vary the plateau length and show the pressure profile along the contact. Note that the slope and the jump are kept constant and as a consequence the local Weissenberg number (i.e., $Wi = \frac{\lambda U}{\Delta h}$) do not change with the profile. The maximum pressure is for the intermediate value of $\ell$, i.e., $\ell = 0.5$.

Upon entering the channel, the polymer is subjected to shearing forces and undergoes stretching (extension). However, it adjusts to this shear when the plateau is long, consequently, also leading to the highest gain in load, as evidenced from Fig. 9(c) that compared the load versus the plateau length. As we reduce the plateau width, we find an earlier onset of relaxation (since the channel diverges, leading to a lower shear strain rate). This causes a decrease in load. Note that the pressure values do not reflect this effect. This is because the room for the stress advection or relaxation plays a key role in breaking the symmetry of the pressure profile which upon summation, yields a net positive force. In the EHL case, the deformation under viscoelastic effects occurs until the applied load is balanced by the film pressure [24]. Therefore, we expect the continued flattening of the surface to further enhance the increment in load due to viscoelasticity. Finally, in Fig. 9(d), we show the distribution of the streamwise polymer normal stress along the channel for different plateau lengths. In each case, it acquires the same value across the channel inlet and outlet, since the step depth is quite small. However, the maximum value predictably spans a larger region dependent on the length of the plateau.

## 4. Conclusions

This study examines the distribution of pressure and stress along a steep converging/diverging channel. The geometry is modeled via a tangent hyperbolic step function in two separate analyses. First, we examine only a converging or diverging step, therefore having different channel entrance and exit heights. Secondly, we mimic an EHL profile by mixing two step functions thereby creating a channel with a plateau and identical height for entrance and exit.

We observe a strong influence of the position and height of the step on the pressure distribution and load carrying capacity at the onset of viscoelasticity. While the Newtonian load can be positive or negative depending on the sign of $\Delta h$, the polymer streamwise normal stresses can generate additional forces depending on both the location and height of the step. Ideally, when the step is located at the center of the channel, a maximum in the load is observed, which, interestingly, tends to decline as viscoelasticity is strengthened. However, when placing a converging step close to the inlet (outlet), the load falls below the maximum, but increases (decreases) versus $De$. The placement of the

step, therefore, plays a key role in improving not only the maximum load carrying capacity but also its dependence on viscoelasticity. On the other hand, when the channel is diverging, i.e., $\Delta h < 0$, we observe the opposite effect and trends versus $De$.

For a viscoelastic flow, the normal force along the channel inlet and outlet open boundaries must be balanced, leading to a pressure condition dependent on the average normal stress. Accounting for this, we observe a large overall increase in the pressure due to finite streamwise normal stresses that scale with the Deborah number. It is interesting to note that for the sliding case, the normal stresses at the boundaries are finitely large ($De > 0$) and, when added to the pressure, will always yields a load increment.

The results illustrated in this article can shed light on the positive effect of fluid viscoelasticity in soft lubricated contacts [24]. However, due to the simplicity of the examined geometries, can also be used as starting point for analysis for rough or textured profiles [21,34]. In particular, the capability of viscoelasticity of enhancing the load in sudden variation of height as illustrated in this paper could be exploited to design ad-hoc engineered surfaces able to maximize the tribological performance of contacts lubricated with viscoelastic fluids.

## CRediT authorship contribution statement

**M.H. Sari:** Writing – original draft, Validation, Software, Methodology, Data curation. **H. Ahmed:** Writing – review & editing, Supervision. **C. Putignano:** Writing – review & editing, Data curation. **G. Carbone:** Writing – review & editing, Formal analysis, Conceptualization. **L. Biancofiore:** Writing – review & editing, Supervision, Resources, Project administration, Funding acquisition.

## Declaration of competing interest

The authors declare the following financial interests/personal relationships which may be considered as potential competing interests: Luca Biancofiore reports financial support was provided by Scientific and Technological Research Council of Turkey. If there are other authors, they declare that they have no known competing financial interests or personal relationships that could have appeared to influence the work reported in this paper.

## Acknowledgments

MHS, HA and LB would like to acknowledge the Turkish National Research Agency (TÜBİTAK) for supporting this work under the project 221N576. The authors would like also to acknowledge the anonymous referee for the discussions on the stress boundary conditions useful to improve the paper.

## Appendix A. Stress boundary conditions

At the inlet of the upper wall, i.e., $(x = 0, y = h)$, the Oldroyd-B stresses (see Eqs. (5)d-f) are simplified by knowing that $v$ is zero in the bulk region. This is shown as:

$$\frac{du}{dx}(0,h) = \frac{\partial u}{\partial x} + h'\frac{\partial u}{\partial y} = 0, \quad \Rightarrow \frac{\partial u}{\partial x}(0,h) = 0 \tag{21a}$$

$$\frac{dv}{dx}(0,h) = \frac{\partial v}{\partial x} + h'\frac{\partial v}{\partial y} = 0, \quad \Rightarrow \frac{\partial v}{\partial x}(0,h) = 0 \tag{21b}$$

where $h' = \frac{dh}{dx} = 0$ for the inlet flat channel. At the bottom wall, for a constant velocity along $x$, $\frac{\partial u}{\partial x} = 0$, by imposing continuity $\frac{\partial u}{\partial x} + \frac{\partial v}{\partial y} = 0$, we can obtain

$$\left.\frac{\partial v}{\partial y}\right|_{x=0,\, y=0} = 0 \quad \text{and} \quad \left.\frac{\partial v}{\partial y}\right|_{x=0,\, y=h} = 0 \quad \Rightarrow v|_{x=0,y} = 0 \tag{22}$$

Then Eqs. (5)d-f are simplified to

$$\tau_{xx} + De\left(u\frac{\partial \tau_{xx}}{\partial x} - 2\tau_{xy}\frac{\partial u}{\partial y}\right) = 0, \tag{23a}$$

$$\tau_{xy} + De\left(u\frac{\partial \tau_{xy}}{\partial x} - \tau_{yy}\frac{\partial u}{\partial y}\right) = (1-\beta)\frac{\partial u}{\partial y}, \tag{23b}$$

$$\tau_{yy} + De\left(u\frac{\partial \tau_{yy}}{\partial x}\right) = 0, \tag{23c}$$

at $x = 0$, for all $y$. We assume that, at the entry, the polymers originate from a sufficiently long, flat channel where the pressure gradient is same of the inlet. By expanding Eqs. (23) up to the first order in $De$, we obtain a shear dependent solution

$$\begin{bmatrix}\tau_{xx}(0,y)\\ \tau_{xy}(0,y)\\ \tau_{yy}(0,y)\end{bmatrix} = \begin{bmatrix}2De(1-\beta)(\frac{\partial u}{\partial y})^2\\ (1-\beta)\frac{\partial u}{\partial y}\\ 0\end{bmatrix}, \tag{24}$$

which is similar to the entry boundary conditions of Ref. [29]. Applying Eqs. (24) is equivalent to using Neumann boundary conditions $\frac{\partial}{\partial x}\boldsymbol{\tau} = 0$.

For the upper wall ($x = h$), we can write similarly to Eqs. (21) but along the channel

$$\frac{du}{dx}(x,h) = \frac{\partial u}{\partial x} + h'\frac{\partial u}{\partial y} = 0, \ \Rightarrow \frac{\partial u}{\partial x} = -h'\frac{\partial u}{\partial y} \tag{25a}$$

$$\frac{dv}{dx}(x,h) = \frac{\partial v}{\partial x} + h'\frac{\partial v}{\partial y} = 0, \ \Rightarrow \frac{\partial v}{\partial x} = -h'\frac{\partial v}{\partial y}. \tag{25b}$$

By using the continuity equation we have $\frac{\partial v}{\partial y} = h'\frac{\partial u}{\partial y}$ and $\frac{\partial v}{\partial x} = -h'^2\frac{\partial u}{\partial y}$. Inserting these expressions into Eqs. (5)e-f, and noting that both $u$ and $v$ are zero along the wall, we can simplify the linear set of equations to reach

$$\begin{pmatrix}1+2De\,h'\frac{\partial u}{\partial y} & -2De\frac{\partial u}{\partial y} & 0\\ De\,h'^2\frac{\partial u}{\partial y} & 1 & -De\frac{\partial u}{\partial y}\\ 0 & 2De\,h'^2\frac{\partial u}{\partial y} & 1-2De\,h'\frac{\partial u}{\partial y}\end{pmatrix}\begin{pmatrix}\tau_{xx}(x,h)\\ \tau_{xy}(x,h)\\ \tau_{yy}(x,h)\end{pmatrix} = \begin{pmatrix}0\\ (1-\beta)\frac{\partial u}{\partial y}\\ 2(1-\beta)h'\frac{\partial u}{\partial y}\end{pmatrix}. \tag{26}$$

where Eq. (8) is solution of the Eq. (26).

## Appendix B. Linearized solution (LIN)

In this appendix we report the expressions for the linearized in $De$ solution for the velocity field that is needed for our VR algorithm. More details can be found in Refs. [20,21,24]. The velocity field, pressure and stress fields are perturbed with respect to $De$ number up to the first order

$$\boldsymbol{u} = \boldsymbol{u}^{(0)} + De\boldsymbol{u}^{(1)} + O(De^2), \tag{27a}$$

$$p = p^{(0)} + Dep^{(1)} + O(De^2), \tag{27b}$$

$$\boldsymbol{\tau} = \boldsymbol{\tau}^{(0)} + De\boldsymbol{\tau}^{(1)} + O(De^2). \tag{27c}$$

Placing Eqs. (27a)–(27c) into the reduced momentum and continuity equations (Eqs. (5)) the zero-th order

$$u^{(0)} = \frac{1}{2}\frac{dp^{(0)}}{dx}\left(y^2 - yh\right) + 1 - \frac{y}{h} \tag{28a}$$

$$v^{(0)} = \frac{1}{12}\frac{d^2p^{(0)}}{dx^2}\left(2y^3 - 3y^2h\right) + \frac{y^2}{4}\frac{dp^{(0)}}{dx}\frac{dh}{dx} - \frac{y^2}{2h^2}\frac{dh}{dx} \tag{28b}$$

$$\frac{d}{dx}\left(h^3\frac{p^{(0)}}{dx}\right) = 6\frac{dh}{dx} \tag{28c}$$

and first order pressure and velocities can be obtained (see the equation in Box I).

where the variable $h_m$ is the maximum pressure location $h_m = \frac{\int_0^1 h^{-2}}{\int_0^1 h^{-3}}$. The first-order mass flow rate given as:

$$q^{(1)} = \left\{\frac{3}{8}\left(\frac{h_m^2}{h_1^4} - \frac{h_m^2}{h_0^4}\right) - \frac{1}{2}\left(\frac{h_m}{h_1^3} - \frac{h_m}{h_0^3}\right) + \frac{1}{6}\left(\frac{1}{h_1^2} - \frac{1}{h_0^2}\right)\right\} \times \left(\int_0^1 \frac{1}{h^3(s)}ds\right)^{-1}. \tag{30}$$

$$u^{(1)} = (yh - y^2)\left(\frac{(1-\beta)h^2}{8}\frac{dp^{(0)}}{dx}\frac{d^2p^{(0)}}{dx^2} + \frac{(1-\beta)h}{8}\frac{dh}{dx}\left(\frac{dp^{(0)}}{dx}\right)^2 - \frac{(1-\beta)}{4}\frac{d^2p^{(0)}}{dx^2} - \frac{(1-\beta)}{2h^3}\frac{dh}{dx} - \frac{1}{2}\frac{dp^{(1)}}{dx}\right) \tag{29a}$$

$$v^{(1)} = y^3\left(\frac{(1-\beta)h^2\frac{dp}{dx}\frac{d^3p}{dx^3} + (1-\beta)h^2\left(\frac{d^2p}{dx^2}\right)^2 + (1-\beta)h\frac{d^2h}{dx^2}\left(\frac{dp}{dx}\right)^2 + (1-\beta)\left(\frac{dh}{dx}\right)^2\left(\frac{dp}{dx}\right)^2}{24}\right) +$$
$$y^3\left(\frac{(1-\beta)h\frac{dh}{dx}\frac{dp}{dx}\frac{d^2p}{dx^2}}{6} - \frac{(1-\beta)\frac{d^3p}{dx^3}}{12} - \frac{(1-\beta)\frac{d^2h}{dx^2}}{6h^3} + \frac{(1-\beta)\left(\frac{dh}{dx}\right)^2}{2h^4} - \frac{\frac{d^2p^D}{dx^2}}{6}\right) +$$
$$y^2\left(-\frac{(1-\beta)h^3\frac{dp}{dx}\frac{d^3p}{dx^3} + (1-\beta)h^3\left(\frac{d^2p}{dx^2}\right)^2 + 5(1-\beta)h^2\frac{dh}{dx}\frac{dp}{dx}\frac{d^2p}{dx^2} + (1-\beta)h^2\frac{d^2}{dx^2}h\left(\frac{dp}{dx}\right)^2}{16}\right) + \tag{29b}$$
$$y^2\left(\frac{(1-\beta)h\frac{d^3p}{dx^3} + (1-\beta)\frac{dh}{dx}\frac{d^2p}{dx^2} - (1-\beta)h\left(\frac{dh}{dx}\right)^2\left(\frac{dp}{dx}\right)^2}{8} + \frac{(1-\beta)\frac{d^2h}{dx^2}}{4h^2} - \frac{(1-\beta)\left(\frac{dh}{dx}\right)^2}{2h^3} + \frac{h\frac{d^2p^{(1)}}{dx^2}}{4} + \frac{\frac{dh}{dx}\frac{dp^{(1)}}{dx}}{4}\right)$$

$$\frac{d}{dx}\left(h^3\frac{dp^{(1)}}{dx}\right) = (1-\beta)\frac{d}{dx}\left(\frac{dh}{dx}\left(1-3\frac{h_m}{h}\right)\left(2-3\frac{h_m}{h}\right)\right), \tag{29c}$$

**Box I.**

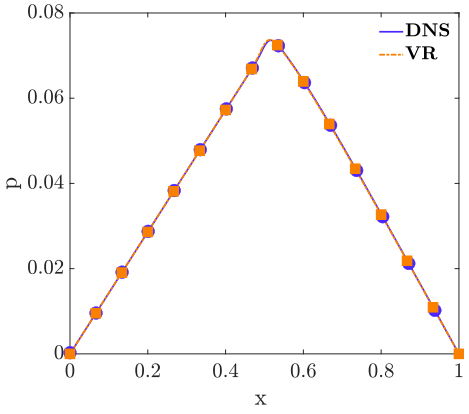


**Fig. 10.** A comparison of the pressure distribution between DNS and VR for the step configuration using $a = 0.5$, $De = 0.1$, $\epsilon = 0.004$ and $\Delta h = 0.025$. The boundary conditions for OpenFOAM are depicted in Eqs. (6a), (6b), (6c), (7) and (8). We used $N_x, N_y = 1024 \times 64$ nodes along the $x$ and $y$ directions in OpenFOAM after checking mesh independency.

## Appendix C. Numerical details and validation

In this section, we validate the viscoelastic Reynolds approach by comparing the results against those obtained via the direct numerical simulations (DNS) of Eqs. (1)–(3) using the RheoTool library in OpenFOAM [39]. This tool leverages the log-conformation-representation which delays the high Weissenberg number problem (HWNP), typical of simulations of viscoelastic fluids, allowing to reach larger values of $De$ [40]. Furthermore, satisfying the requirements for numerical stability leads to very small time step sizes. In contrast, using the VR approach significantly alleviates the HWNP and relaxes the numerical constraint. In Fig. 10, we show how VR gives a good agreement with the DNS for $De = 0.1$ for a step profile with $a = 0.5$ and $\Delta h = 0.025$.

For VR, mesh independent results are achieved using $N_x, N_y = 256{\times}32$ nodes along the $x$ and $y$ directions, respectively, and a time step size of $\Delta t = 3 \times 10^{-3}$. Upon reaching a tolerance $\|\tau_{ij}^{t+\Delta t} - \tau_{ij}^{t}\|^2 < 10^{-11}$ for all the components of the stress, the semi-implicit time marching algorithm stops.

## Data availability

Data will be made available on request.

## References

[1] R.B. Bird, P.J. Dotson, N.L. Johnson, Polymer solution rheology based on a finitely extensible bead—spring chain model, J. Non-Newton. Fluid Mech. 7 (2) (1980) 213–235.
[2] A. Venkatesh, V. Anand, V. Narsimhan, Peeling of linearly elastic sheets using complex fluids at low Reynolds numbers, J. Non-Newton. Fluid Mech. 309 (2022) 104916.
[3] M.A. Alves, P.J. Oliveira, F.T. Pinho, Numerical methods for viscoelastic fluid flows, Annu. Rev. Fluid Mech. 53 (1) (2021) 509–541.
[4] S.S. Datta, A.M. Ardekani, P.E. Arratia, A.N. Beris, I. Bischofberger, G.H. McKinley, J.G. Eggers, J.E. López-Aguilar, S.M. Fielding, A. Frishman, M.D. Graham, J.S. Guasto, S.J. Haward, A.Q. Shen, S. Hormozi, A. Morozov, R.J. Poole, V. Shankar, E.S.G. Shaqfeh, H. Stark, V. Steinberg, G. Subramanian, H.A. Stone, Perspectives on viscoelastic flow instabilities and elastic turbulence, Phys. Rev. Fluids 7 (8) (2022) 080701.
[5] C. Datt, B. Nasouri, G.J. Elfring, Two-sphere swimmers in viscoelastic fluids, Phys. Rev. Fluids 3 (2018) 123301.
[6] R.G. Larson, CHAPTER 8 - Viscoelasticity of Dilute Polymer Solutions, in: R.G. Larson (Ed.), Constitutive Equations for Polymer Melts and Solutions, in: Butterworths Series in Chemical Engineering, Butterworth-Heinemann, 1988, pp. 219–270.
[7] R. Fattal, R. Kupferman, Constitutive laws for the matrix-logarithm of the conformation tensor, J. Non-Newton. Fluid Mech. 123 (2–3) (2004) 281–285.
[8] M.A. Alves, P.J. Oliveira, F.T. Pinho, On the effect of contraction ratio in viscoelastic flow through abrupt contractions, J. Non-Newton. Fluid Mech. 122 (1–3) (2004) 117–130.
[9] L.L. Ferrás, A.M. Afonso, M.A. Alves, J.M. Nóbrega, F.T. Pinho, Newtonian and viscoelastic fluid flows through an abrupt 1:4 expansion with slip boundary conditions, Phys. Fluids 32 (4) (2020) 043103.
[10] J.P. Rothstein, G.H. McKinley, Extensional flow of a polystyrene Boger fluid through a 4 : 1 : 4 axisymmetric contraction/expansion, J. Non-Newton. Fluid Mech. 86 (1–2) (1999) 61–88.
[11] M.A. Alves, R.J. Poole, Divergent flow in contractions, J. Non-Newton. Fluid Mech. 144 (2) (2007) 140–148.
[12] D.V. Boger, Viscoelastic flows through contractions, Annu. Rev. Fluid Mech. 19 (1987) 157–182.

[13] A.P. Koppol, R. Sureshkumar, A. Abedijaberi, B. Khomami, Anomalous pressure drop behaviour of mixed kinematics flows of viscoelastic polymer solutions: a multiscale simulation approach, J. Fluid Mech. 631 (2009) 231–253.
[14] M.A. Alves, P.J. Oliveira, F.T. Pinho, Benchmark solutions for the flow of Oldroyd-B and PTT fluids in planar contractions, J. Non-Newton. Fluid Mech. 110 (1) (2003) 45–75.
[15] Spatial decay of steady perturbations of plane Poiseuille flow for the Oldroyd-B equation, 46.
[16] R.A. Keiller, Entry-flow calculations for the Oldroyd-B and FENE equations, J. Non-Newton. Fluid Mech. 46 (2–3) (1993) 143–178.
[17] D.M. Binding, P.M. Phillips, T.N. Phillips, Contraction/expansion flows: The pressure drop and related issues, J. Non-Newton. Fluid Mech. 137 (1–3) (2006) 31–38.
[18] R.J. Poole, M.A. Alves, P.J. Oliveira, F.T. Pinho, Plane sudden expansion flows of viscoelastic liquids, J. Non-Newton. Fluid Mech. 146 (1) (2007) 79–91, 3rd Annual European Rheology Conference.
[19] B. Debbaut, J.M. Marchal, M.J. Crochet, Numerical simulation of highly viscoelastic flows through an abrupt contraction, J. Non-Newton. Fluid Mech. 29 (1988) 119–146.
[20] J.A. Tichy, Non-Newtonian lubrication with the convected Maxwell model, J. Tribol. 118 (2) (1996) 344–348.
[21] S.S. Gamaniel, D. Dini, L. Biancofiore, The effect of fluid viscoelasticity in lubricated contacts in the presence of cavitation, Tribol. Int. 160 (2021) 107011.
[22] E. Boyko, H.A. Stone, Flow rate–pressure drop relation for shear-thinning fluids in narrow channels: approximate solutions and comparison with experiments, J. Fluid Mech. 923 (2021) R5.
[23] K.D. Housiadas, A.N. Beris, Lubrication approximation of pressure-driven viscoelastic flow in a hyperbolic channel, Phys. Fluids 35 (12) (2023) 123116.
[24] M.H. Sari, C. Putignano, G. Carbone, L. Biancofiore, The effect of fluid viscoelasticity in soft lubrication, Tribol. Int. 195 (2024) 109578.
[25] E. Boyko, H.A. Stone, Reciprocal theorem for calculating the flow rate–pressure drop relation for complex fluids in narrow geometries, Phys. Rev. Fluids 6 (8) (2021) L081301.
[26] H. Ahmed, L. Biancofiore, A new approach for modeling viscoelastic thin film lubrication, J. Non-Newton. Fluid Mech. 292 (2021) 104524.
[27] H. Ahmed, L. Biancofiore, Modeling polymeric lubricants with non-linear stress constitutive relations, J. Non-Newton. Fluid Mech. 321 (2023) 105123.
[28] R.G. Owens, T.N. Phillips, Computational Rheology, Imperial College Press, 2002.
[29] E. Boyko, J. Hinch, H.A. Stone, Flow of an Oldroyd-B fluid in a slowly varying contraction: theoretical results for arbitrary values of Deborah number in the ultra-dilute limit, J. Fluid Mech. 988 (2024) A10.
[30] J. Hinch, E. Boyko, H.A. Stone, Fast flow of an Oldroyd-B model fluid through a narrow slowly varying contraction, J. Fluid Mech. 988 (2024) A11.
[31] K.D. Housiadas, A.N. Beris, Pressure-drop and Trouton ratio for Oldroyd-B fluids in hyperbolic converging channels, Phys. Fluids 36 (2) (2024) 021702.
[32] S.C. Vladescu, A.V. Olver, I.G. Pegg, T. Reddyhoff, The effects of surface texture in reciprocating contacts–an experimental study, Tribol. Int. 82 (2015) 28–42.
[33] L. Biancofiore, M. Giacopini, D. Dini, Interplay between wall slip and cavitation: A complementary variable approach, Tribol. Int. 137 (2019) 324–339.
[34] M.Y. Çam, M. Giacopini, D. Dini, L. Biancofiore, A numerical algorithm to model wall slip and cavitation in two-dimensional hydrodynamically lubricated contacts, Tribol. Int. 184 (2023) 108444.
[35] B.J. Hamrock, S.R. Schmid, B.O. Jacobson, Fundamentals of Fluid Film Lubrication, CRC Press, 2004.
[36] E. Boyko, H.A. Stone, I.C. Christov, Flow rate-pressure drop relation for deformable channels via fluidic and elastic reciprocal theorems, Phys. Rev. Fluids 7 (9) (2022) L092201.
[37] R.I. Tanner, Engineering Rheology, vol. 52, OUP Oxford, 2000.
[38] X.K. Li, Y. Luo, Y. Qi, R. Zhang, On non-Newtonian lubrication with the upper convected Maxwell model, Appl. Math. Model. 35 (5) (2011) 2309–2323.
[39] F. Pimenta, M. Alves, Stabilization of an open-source finite-volume solver for viscoelastic fluid flows, J. Non-Newton. Fluid Mech. 239 (2017) 85–104.
[40] R. Fattal, R. Kupferman, Time-dependent simulation of viscoelastic flows at high Weissenberg number using the log-conformation representation, J. Non-Newton. Fluid Mech. 126 (1) (2005) 23–37.